Journal of MATERIALS RESEARCH

Invited Feature Paper-Review
DOI:10.1557/s43578-021-00397-x

ULTRA-WIDE BANDGAP MATERIALS, DEVICES, AND SYSTEMS

FOCUS ISSUE

Gallium oxide-based optical nonlinear effects and photonics devices

Jingan Zhou[1,2], Hong Chen[3], Kai Fu[1,2], Yuji Zhao[1,2,a)]

[1] School of Electrical, Computer and Energy Engineering, Arizona State University, Tempe, AZ 85287, USA
[2] Department of Electrical and Computer Engineering, Rice University, Houston, TX 77005, USA
[3] Max Planck Institute of Microstructure Physics, Weinberg 2, 06120 Halle (Saale), Germany
[a)] Address all correspondence to this author. e-mail: yuji.zhao@rice.edu

Received: 2 June 2021; accepted: 20 September 2021; published online: 21 October 2021

Photonics devices working in the ultraviolet and visible (UV–Vis) spectra have drawn great attention due to their potential applications in the optical computing, communication, and bio-chemical sensing fields. Due to its wide bandgap, broadband transparency, low cost, and high thermal/chemical stability, gallium oxide (Ga_2O_3) semiconductor has emerged as a new platform for UV–Vis nonlinear optics and integrated photonics. In this paper, we review the recent studies on its nonlinear properties and applications for photonic devices. First, we introduce its different polymorphs and growth methods. Second, we present its basic optical properties. Third, we discuss its optical nonlinear effects including two-photon absorption, optical Kerr effect, photoluminescence, and Raman effect. Finally, we discuss the recent progress of photonics and optoelectronic devices based on Ga_2O_3 including waveguides and photodetectors. With the rapid development of Ga_2O_3 technologies, we fully expect more advanced photonic devices emerging on this exciting new photonic material platform.

Introduction

Si photonics has attracted considerable attention for integrated photonics applications due to their outstanding optical performance as well as the excellent compatibility with the mature CMOS processes [1, 2]. However, the relatively narrow bandgap of Si (e.g., 1.1 eV) has fundamentally limited the optical performance of Si devices in the ultraviolet and visible (UV–Vis) spectra, which greatly hindered the applications in frequency metrology [3, 4], on-chip mode-locking [5], visible light communications [6, 7], and deep-brain optical stimulation [8, 9], where the transmission of UV–Vis spectra is required. To extend the working wavelengths into the UV–Vis spectra, wide and ultra-wide bandgap materials, such as GaN, SiC, diamond, and AlN, are attracting increasing interests. Recently, a new class of ultra-wide bandgap semiconductor Ga_2O_3 has emerged with many excellent material properties for both electronic, e.g., power devices [10], and photonics applications, e.g., solar-blind photodetectors [11, 12]. Ga_2O_3 has unique properties that are promising for photonic applications in the UV–Vis spectra. For example, the wide bandgap of β-Ga_2O_3 (4.88 eV) [13] provides broadband transparency and a small two-photon coefficient (β_{TPA} = 0.6 cm/GW at 400 nm) [14], which allows weak photon absorptions. It also has a small lattice mismatch with the III-N material system, which is preferable for the active integration of III-N lasers and detectors. To date, large-scale high-quality Ga_2O_3 wafers and epitaxial thin films are commercially available at low cost, which has laid foundation for the device development. Consequently, high-performance optical devices have been successfully demonstrated on Ga_2O_3 materials, including low loss Ga_2O_3 waveguide (3.7 dB/cm) and photodetectors with high responsibility (230 A/W).

In this article, we review the recent studies on the nonlinear optical properties in Ga_2O_3, and discuss their potential applications for optical and photonic devices. The article is divided into four main sections. The first section introduces the different polymorphs and growth methods of Ga_2O_3 bulk crystals and epitaxial thin films. The second section presents the basic optical properties of Ga_2O_3 including band structure, refraction index, transmission, and absorption. The third section discusses optical nonlinear effects of Ga_2O_3 including two-photon absorption, optical Kerr effect, photoluminescence, and Raman effect. Finally, the fourth section will discuss the recent progress

of photonics and optoelectronic devices based on Ga_2O_3. The outline is shown in Fig. 1 to help the readers understand this article (Fig. 2).

Polymorphism and growth

Before we discuss the optical properties of Ga_2O_3, it is very important to introduce the different crystals of Ga_2O_3 as well as their growth methods, which have significant impacts on their optical properties. To date six polymorphs of Ga_2O_3 have been theoretically predicted by first-principles calculations and experimentally demonstrated. These polymorphs (α, β, γ, ε, δ and κ) have different crystallographic structures and growth conditions. Table 1 summarizes their crystal systems, space groups, and lattice parameters. Among them, β-Ga_2O_3 is the most stable phase. It is the only phase that can be grown directly from the melt Ga_2O_3, which makes it the widest-researched Ga_2O_3 polymorph for both electronics and photonics applications.

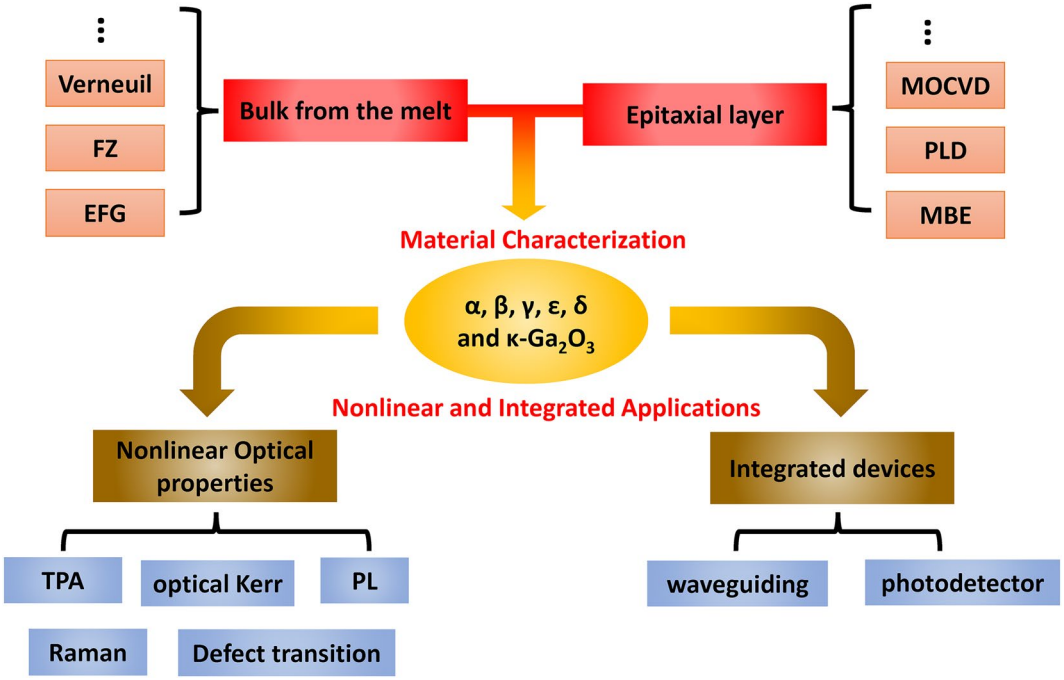

Figure 1: Summary of the key words and the outline of the article. This paper introduces the progress of Ga_2O_3 from the material preparation and characterization to the nonlinear and integrated applications.

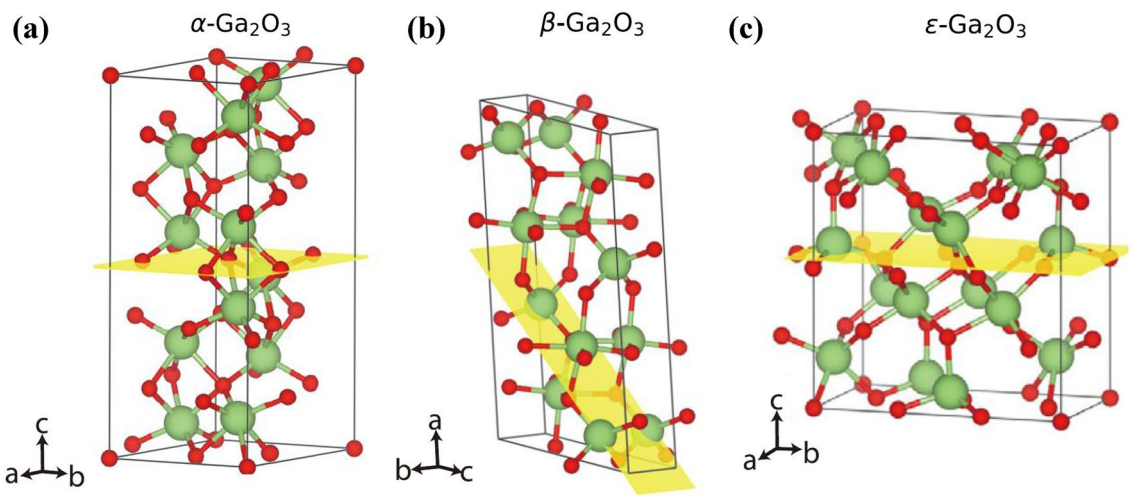

Figure 2: Atomic crystalline structure of different Ga_2O_3 phases along the preferred lattice orientation on a hexagonal substrate. Green and red atoms represent gallium and oxygen atoms, respectively. The yellow plane represents the growth plane. (a) Trigonal α-Ga_2O_3 (b) Monoclinic β-Ga_2O_3 (c) Hexagonal ε-Ga_2O_3. These figures were reprinted from Ref. [19], with the permission of AIP Publishing.

Other polymorphs are the metastable phases and have not been reported to be grown from the melt Ga_2O_3. Furthermore, Playford et al. [15] reported that the δ-Ga_2O_3 may be a nanocrystalline modification of ε-Ga_2O_3 using neutron total diffraction analysis. Cora et al. [16] reported that κ-Ga_2O_3 is likely to be misinterpreted as ε-Ga_2O_3 if the ordered domain size falls below the actual resolution of the probing techniques. Other polymorphs are the metastable phases and have not been reported to be grown from the melt Ga_2O_3.

β-Ga_2O_3, the most stable form of Ga_2O_3, has a monoclinic crystal structure in the C2/m space group. Its unit cell consists of four Ga_2O_3 chemical formula units with two kinds of Ga atoms and three kinds of O atoms. Ga(I) and Ga(II) atoms are caged in an oxygen atom tetrahedron and an oxygen atom octahedron, respectively. O(I) and O(II) are threefold coordinated, while O (III) is fourfold coordinated. Due to their recent success in electronics devices, there is a growing interest in the β-Ga_2O_3 optics and photonics devices. And nonlinear optical effects such as two-photon absorption and Kerr effect have been reported on β-Ga_2O_3 [14]. These results will be introduced in detail in the following sections.

In addition to β-Ga_2O_3, other polymorphisms, such as *α* and *ε*, are also attracting increasing interests for both photonics and electronics applications. The metastable phase ε-Ga_2O_3 has an orthorhombic crystal structure in the hexagonal $P6_3mc$ space group, which is a basis transformation from the hexagonal lattice. The oxygen atoms layers form the close-packed stacking in an ABAC sequence. The gallium atoms occupy octahedral and tetrahedral oxygen cavities in the interlayers, forming two types of polyhedral layers parallel to (001). The edge-sharing octahedra and the corner-sharing tetrahedra connect to form zig-zag chains along the [100] direction. Gottschalch et al. [17] reported α-, κ-, β-, ε- and γ-Ga_2O_3 can be deposited heteroepitaxially by metalorganic vapor phase epitaxy (MOVPE) on various substrates. Due to its hexagonal structure, the ε-Ga_2O_3 has less lattice mismatch with the hexagonal substrate. Furthermore, Yoshioka et al. [18] calculated the Helmholtz free energy as a function of temperature for the five different Ga_2O_3 phases, and reported ε- is the second most stable form of Ga_2O_3 next to the β-phase. Cho et al. [19] also reported that ε-Ga_2O_3, as a metastable polymorphism, can be more stable by the engineering of the in-plane strain with hexagonal and cubic substrates. These results suggest that in addition to β-Ga_2O_3, ε-Ga_2O_3 can also be an important phase for electronic and optical applications. Due to their symmetry, stronger nonlinear effects can be expected from ε-Ga_2O_3, which is a topic of active investigation.

The development of crystal growth and thin film epitaxy techniques for Ga_2O_3 has been very rapid in recent years. To date, high-quality bulk β-Ga_2O_3 single crystals can be successfully grown at large-scale and low production cost from the gas phase, solution, and melt. The dominate melt growth methods include Verneuil method [20], optical floating zone (FZ) [21–23], Czochralski method [24, 25], edge-defined film-fed growth (EFG) [26–29], and Bridgman method [30], which are illustrated in Fig. 3a–d. Furthermore, Ga_2O_3 thin films were successfully grown on the substrate both heteroepitaxially and homoepitaxially by metal organic chemical vapor deposition (MOCVD) [31, 32], halide vapor phase epitaxy (HVPE) [33], chemical vapor deposition (CVD), molecular beam epitaxy (MBE), and pulsed laser deposition (PLD). For example, Yao et al. [31] reported the heteroepitaxially films of β-Ga_2O_3 grown on *c*-plane sapphire (0001) using MOCVD technique, as well as metastable α- and ε-phases using HVPE technique. Egyenes-Pörsök et al. [32] reported the growth of α- and β-Ga_2O_3 on *m*- and *c*-plane sapphire substrate using liquid-injection MOCVD. As shown in Fig. 4, Sun et al. [34] reported the influence of HCl flow to the crystal phases and orientations of Ga_2O_3 thin films on *c*-plane sapphire by MOCVD growth. By continuously increasing the HCl flow, the deposited Ga_2O_3 transformed from β phase to ε phase at 30 sccm of flow and finally stopped in α phase at 60 sccm of flow. The results suggest that HCl performs as a catalyst to narrow the difference in free energy between them and help to form the thermally metastable phase. These successful growth and epitaxy techniques and the resulted high-quality Ga_2O_3 materials laid the solid foundation for optical studies on Ga_2O_3 as well as device demonstrations.

Basic optical properties

Next, we discuss the basic optical properties of Ga_2O_3, which stems from the crystal structure and electronic band of the material. Most of the results to date are focused on β-Ga_2O_3

TABLE 1: Summary of the properties of Ga_2O_3 polymorphs.

Polymorph	Crystal system	Space group	*a* (Å)	*b* (Å)	*c* (Å)	*β* (°)	References
α	Trigonal	$R\bar{3}c$	4.98		13.43		Marezuo et al. [75]
β	Monoclinic	$C2/m$	12.23	3.04	5.80	103.7	Zhang et al. [53]
γ	Cubic	$Fd\bar{3}m$	8.24				Playford et al. [15]
ε	Hexagonal	$P6_3mc$	2.906		9.255		Mezzadri et al. [76]
δ	Cubic	$Ia3$	9.52				Roy et al. [77]
κ	Orthorhombic	$Pna2_1$	5.0463	8.7020	9.2833		Cora et al. [16]

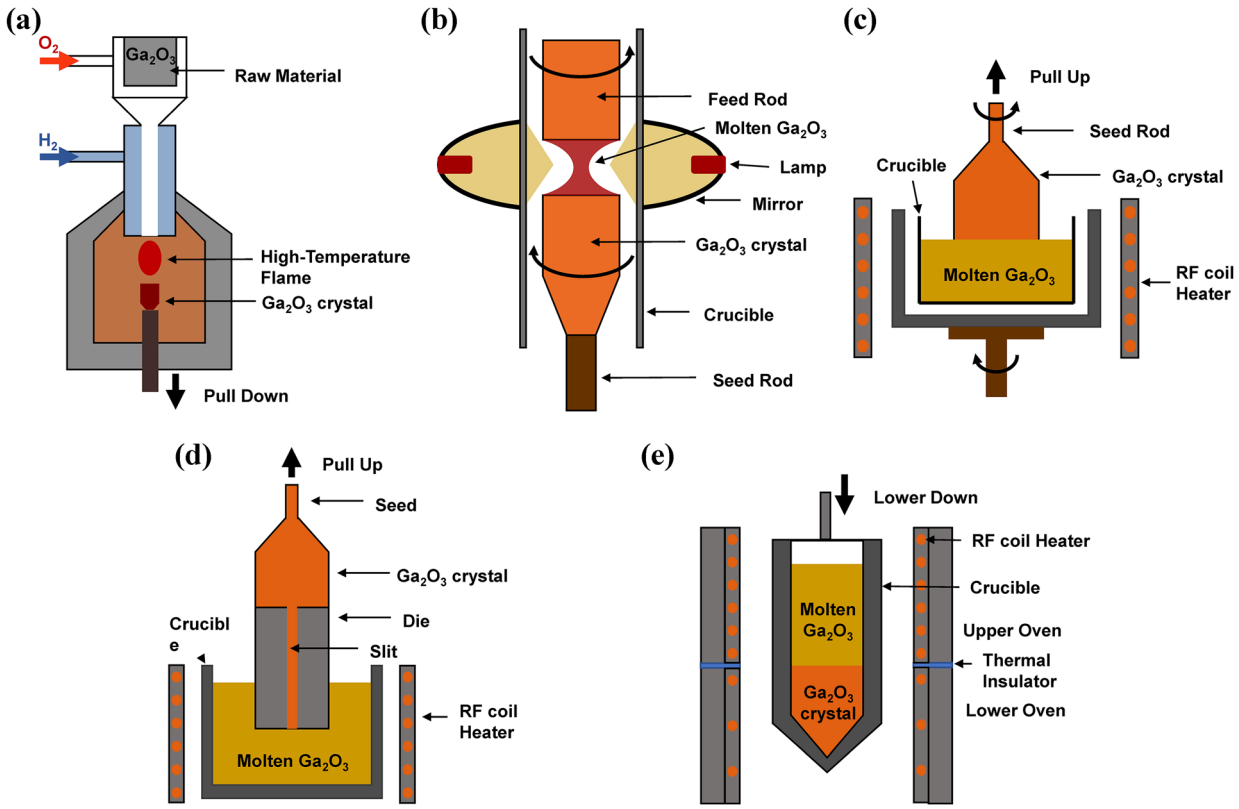

Figure 3: Different growth technologies of bulk β-Ga_2O_3 single crystal from melt Ga_2O_3. Schematic of (a) Verneuil method (b) optical floating zone method (c) Czochralski method (d) edge-defined film-fed growth (e) Bridgman method.

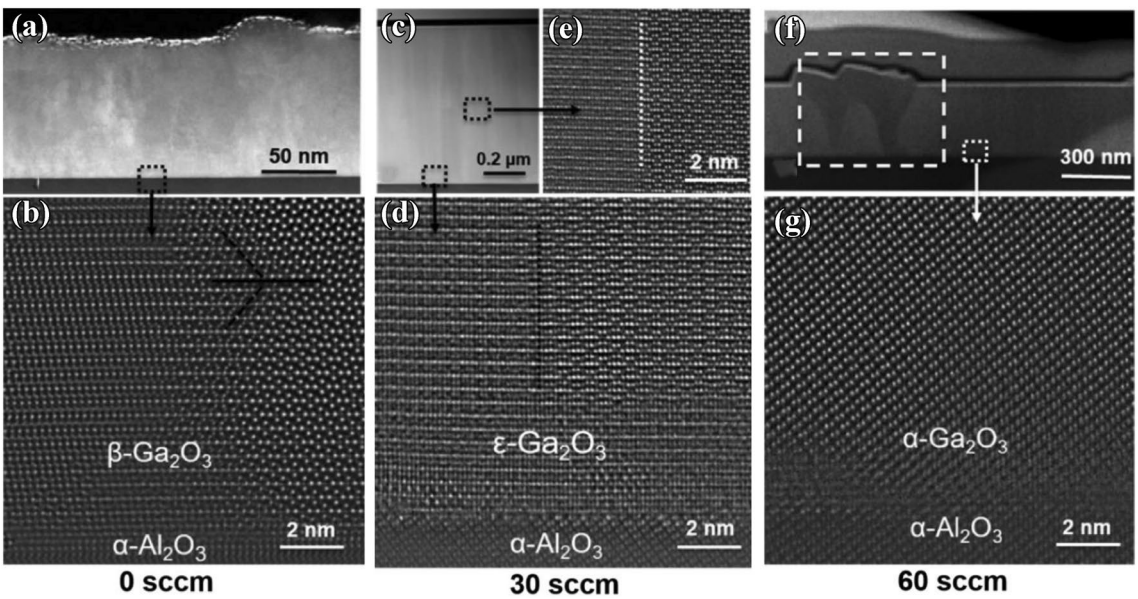

Figure 4: HAADF STEM imaging of FIB cross-sectional samples grown under HCl flow rates of 0, 30, and 60 sccm. The increasing flow of HCl results to the transformation of deposited Ga_2O_3 phase from *β* to ε and then α, (a), (c), (f) Low-intermediate magnification. (b), (d), (g) High-magnification STEM images. (e) Detail at the domain boundary along the film. These figures were reprinted with permission from Ref. [34]. Copyright (2018) American Chemical Society.

due to its high maturity in crystal growth and commercial success in power devices. The basic linear optical properties of both β-Ga_2O_3 bulk crystal and epilayer are well investigated. Due to the wide bandgap, β-Ga_2O_3 provides broadband transparency from UV to near-infrared (NIR) spectra. The electronic band structures of β-Ga_2O_3 were studied by Onuma et al. [35], Peelaers et al. [13], Zhang et al. [36], and Mengle et al. [37]. Figure 5 shows the band structure of β-Ga_2O_3 in the Brillouin zone. The minimum in the conduction band is located at Γ. The location of the maximum in the valance band has not been determined yet. However, since the dispersion of the valance band is quite small, its location does not significantly influence the bandgap. The fundamental bandgap is indirect with a magnitude of 4.84 eV. The Γ point, corresponding to the minimum direct bandgap, is larger than the indirect bandgap by only 0.04 eV (4.88 eV). Considering the momentum conservation, Γ–Γ direct transition is more likely to happen than the indirect transition since the latter requires the participation of phonons. Thus, in most cases, β-Ga_2O_3 can be regarded as a direct bandgap material.

Many studies were performed to explore the basic optical properties of β-Ga_2O_3 such as refractive index, transmittance, and near-edge absorption. For example, the wavelength dependence of the refractive index was measured in bulk β-Ga_2O_3 crystal by Onuma et al. [38]. The anisotropic optical properties of β-Ga_2O_3 were investigated using spectroscopic ellipsometry measurements. As shown in Fig. 6(a), in the visible spectra the refractive index of β-Ga_2O_3 decreases with the photon energy from ~2.1 to ~1.98, and does not show strong anisotropy. In the UV spectra, the anisotropy is distinguishable along *a**-, *b*-, and *c*-axis. The value of the refractive index was found to be smaller than that in the single crystal, which was attributed to the influence of the crystallinity. Furthermore, the temperature dependence of the refraction index was also measured by Bhaumik et al. [39]. Sellmeier coefficients were tabulated for different temperatures in the range of

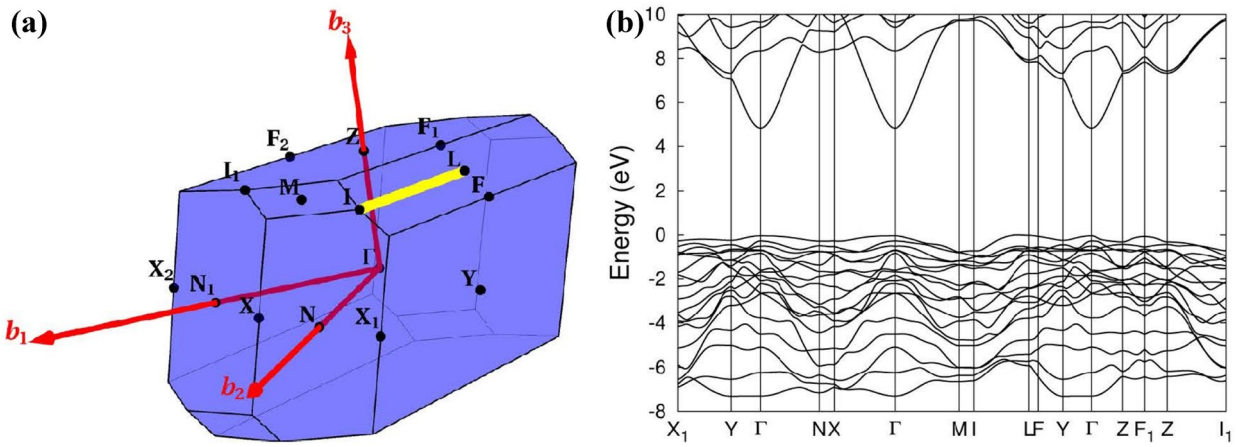

Figure 5: (a) The Brillouin zone corresponding to the relaxed monoclinic β-Ga_2O_3. Labels indicate high-symmetry points. The red arrows show the axes of the reciprocal unit cell. (b) Band structure of β-Ga_2O_3 along a continuous path in the Brillouin zone. The minimum indirect bandgap is located at Γ–Γ transition. These figures were reprinted from Ref. [13], with the permission from Wiley.

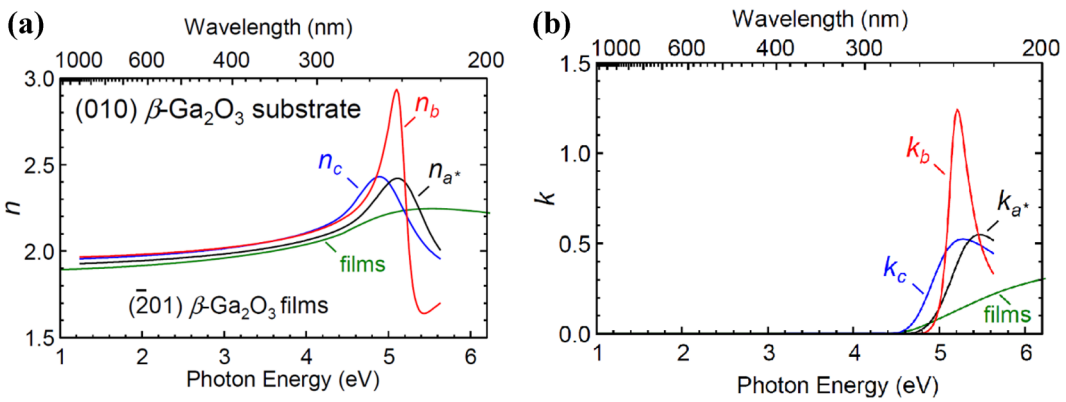

Figure 6: Spectra for (a) refractive index *n* and (b) extinction coefficient k of β-Ga_2O_3 thin film and substrate. In the visible spectra, the refractive index decreases with the photon energy from ~2.1 to ~1.98, and does not show significant anisotropy. Whereas, in the UV spectra, the anisotropy is distinguishable along three different orientations. These figures were reprinted from Ref. [38]. Copyright (2016) The Japan Society of Applied Physics.

30–150 °C. It was found that the refractive index increased linearly with the temperature. The thermal coefficient of the refractive index was found to be at the magnitude of ~10^{-5}/°C and increased towards shorter wavelengths. The results indicate that the β-Ga_2O_3 optical devices working in the UV spectra should be more sensitive to the temperature variations.

The transmittance and near-edge absorption spectra of β-Ga_2O_3 crystal were also measured. For example, transmittance spectra of bulk β-Ga_2O_3 crystal were measured by Zhang et al. [29]. A nominally unintentionally doped crystal showed an optical transmission of higher than 80% in the UV–Vis region, and no obvious decrease was observed in the transmission even in the infrared region. With the increase of Si doping, the transmittance reduced in the UV–Vis region and decreased sharply in the infrared region, which was due to the free carrier absorption.

Since β-Ga_2O_3 reveals significant anisotropic optical properties, the polarization dependence of the band-edge absorption was observed by many researchers. As shown in Fig. 6b, Ricci et al. [40] reported that the lowest absorption edge at 4.54 eV is for polarization E||c, followed by the 4.57 eV for $E||a$ on (010)-oriented sample, and 4.72 eV for $E||b$ on $(\bar{2}01)$-oriented sample. Additionally, the $(\bar{2}01)$-oriented sample showed stronger anisotropy than the (010)-oriented sample, and the absorption edge was shifted towards higher energy by 0.2 eV. The theoretical analysis clearly indicated that the shift in the b onset is due to the suppression of the transition matrix elements in the three top valence bands at Γ point. Furthermore, Mengle et al. [37] used first-principles calculation based on many-body perturbation theory to investigate the near-edge electronic and optical properties of β-Ga_2O_3. According to their calculation, β-Ga_2O_3 has the anisotropy of the absorption onset, which theoretically explained the large range (4.4–5.0 eV) of the experimentally reported band-gap values. Different from the bulk β-Ga_2O_3 with high crystal quality, the transmittances and absorption edges of epitaxial thin film β-Ga_2O_3 depend on the growth temperatures, post-growth heat treatments, doping conditions, and substrate types [41–43]. According to Zhang et al. [41], the absorption edge of the films increases with the increase of crystallinity under different substrate temperatures. An abrupt edge value changing from 4.48 to 5.09 eV occurs when amorphous to crystalline transition is observed.

Nonlinear properties

In addition to the linear optical properties, β-Ga_2O_3 also shows several nonlinear optical effects. In this section, we review the important nonlinear optical effects such as two-photon absorption (TPA), optical Kerr effect, photoluminescence, and Raman scattering. These nonlinear optical properties could be engineered for a wide range of applications such as frequency comb [44], supercontinuum [45], all-optical switch [46] and material characterization. Compared with other wide bandgap materials which can only be grown epitaxially, Ga_2O_3 has the advantage of the low-cost melting growth method, which has led to large scale wafers with high crystal qualities. While our discussions will be focused on β-Ga_2O_3, it is important to note that the emerging ε-Ga_2O_3 has a non-centrosymmetric structure, which could lead to second-order optical nonlinearity. Overall, extensive research is still required to understand the second-order and third-order nonlinearities in β-Ga_2O_3 which are of vital importance for achieving high-performance optical and photonic devices.

Two-photon absorption and Kerr effect

For integrated photonics applications, a pulse laser with high energy will be used to excite the nonlinear effects, which includes the two-photon (TPA) absorption and Kerr effect. The TPA process refers to the significant nonlinear absorption for photon energies between bandgap (E_g) and 1/2 E_g under the high laser intensity. The Kerr is a $\chi^{(3)}$ process which could be used to engineer the dispersion and frequency comb generations [47]. Chen et al. [14] measured the TPA and Kerr effect on the (010) and $(\bar{2}01)$ β-Ga_2O_3 using the Z-scan technique. The experiment results were also compared with simulation results obtained using an analytical model developed by Sheik-Bahae et al. [48]. As shown in Fig. 7. The TPA coefficient was measured to be 1.2 cm/GW for the (010) β-Ga_2O_3, and 0.6 cm/GW for the $(\bar{2}01)$ β-Ga_2O_3. The Kerr nonlinear refractive index was -2.1×10^{-15} cm^2/W for the (010) β-Ga_2O_3, and -2.9×10^{-15} cm^2/W for the $(\bar{2}01)$ β-Ga_2O_3. The TPA coefficient also showed a strong wavelength dependence for β-Ga_2O_3. For the (010) β-Ga_2O_3, the TPA coefficient was found to be larger on $E_\perp$ than the value on $E_{||}$. In comparison, the TPA coefficient was smaller on $E_\perp$. Compared with other wide bandgap semiconductors such as GaN, the TPA coefficient of β-Ga_2O_3 is 20 times smaller, and the Kerr nonlinear refractive index of β-Ga_2O_3 is 4–5 times smaller, than the values on GaN. These results indicate that β-Ga_2O_3 has a high potential for ultra-low loss waveguides and ultra-stable resonators for integrated photonics applications, especially in the UV–Vis spectral range.

Photoluminescence

Photoluminescence (PL) is a nonlinear optical process that is closely related to the electronic structure (band structure), defect state, and impurities of the crystal. The luminescence peaks of the Ga_2O_3 materials are mostly electron transitions from defect energy levels or impurity energy levels. The defect band emissions of Ga_2O_3 crystal are attributed to several gallium vacancies (V_{Ga}), oxygen vacancies (V_O), and gallium-oxygen vacancy pairs (V_{Ga}, V_O). Luminescence spectra in β-Ga_2O_3 crystals excited above the bandgap energy consist of UV (3.2–3.6 eV), blue-green (2.8–3.0 eV), and red (1.6–1.8 eV)

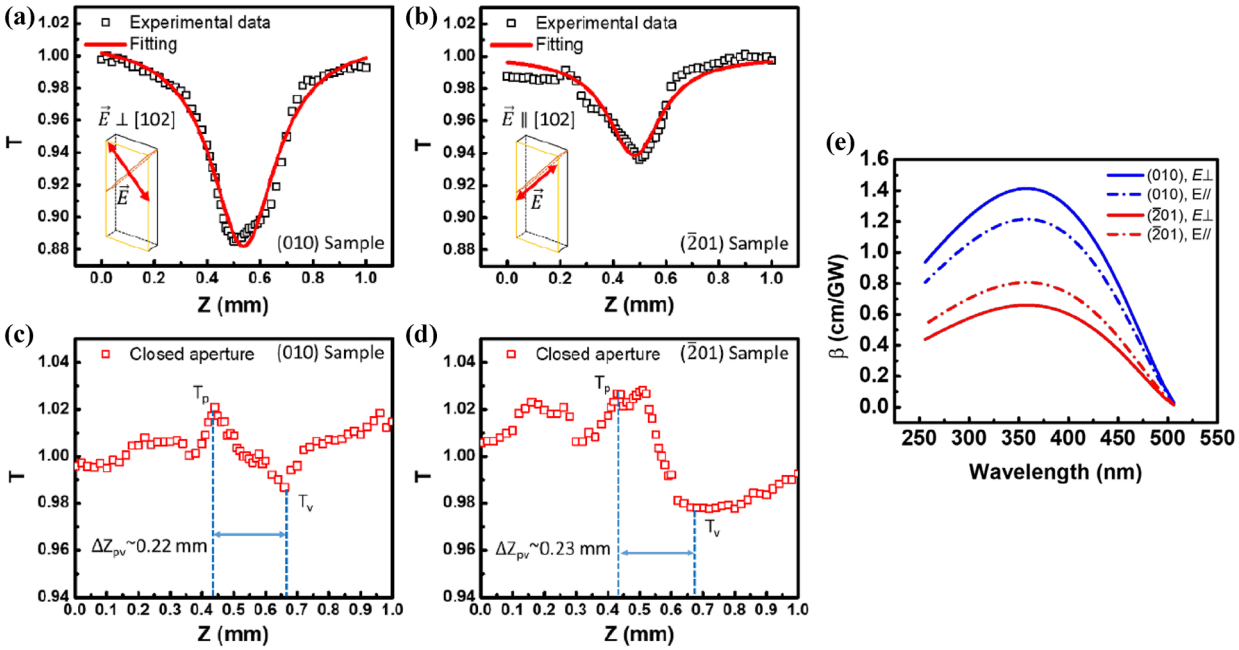

Figure 7: (a–d) Typical open and close aperture scanning curves in the TPA and Kerr effects measurements. (e) The estimated wavelength dependence of TPA coefficient for different β-Ga_2O_3 orientations. These figures were reprinted with permission from Ref. [14] © The Optical Society

broad bands. Studies have shown that the UV emission in β-Ga_2O_3 is an intrinsic recombination transition process attributed to the electrons formed by V_O on the donor and the holes formed by V_{Ga} on the acceptor. They recombine through self-trapping excitation, releasing UV emission bands. The blue emission is caused by the recombination of electrons on the donor and holes on the acceptor, which is due to the V_o, V_{Ga} and V_{Ga}–V_o vaccines. These vaccines are generated during the synthesis of β-Ga_2O_3 under the high temperature. The red emission may result from the change in the band structure of Ga_2O_3 due to the incorporation of C or N from the ambient atmosphere. These impurities will behave as deeper acceptors, and recombine with the electrons captured at the V_o donor to release red emission [49, 50].

To investigate the origin of red emission in β-Ga_2O_3, Naresh-Kumar et al. [51] measured PL spectra of β-Ga_2O_3 samples doped with Sn, Si, and Fe, respectively. At room temperature, the peak positions of the sharp lines for the unintentionally doped (UID) and Fe-doped β-Ga_2O_3 sample are at 693.6 nm and 689.4 nm, respectively. The sharp peaks around 690 nm are caused by the higher concentration of Fe compared with the trace level of Cr in the samples. Particularly in the Fe-doped sample, these red emissions might be related to Fe^{3+} transitions. And the peaks around 688 nm and 695 nm are related to the Cr^{3+} impurities, which can result in a strong luminescence. Furthermore, PL on β-Ga_2O_3 also shows strong temperature dependence. For example, Yamaga et al. [52] reported the optical polarization from the luminescence spectra under different temperatures ranging from 14 to 300 K. When the temperature increases, the UV bands become week and new blue/green bands with two peaks become significant. The polarization of excitement does not change the luminescence spectra. The polarized $E_{em}//c$ and $E_{em}//a$ components dominate in the UV and blue/green bands, respectively, whereas the $E_{em}//b$ components of both bands are weak. In addition, Zhang et al. [53] investigated the temperature-dependent PL on pure phase and highly crystalline β-Ga_2O_3 substrates doped with Si and Mg separately at 77 K, 157 K, 237 K, and 297 K. Figure 8 shows the PL spectra of un-doped β-Ga_2O_3, β-Ga_2O_3:Si, and β-Ga_2O_3:Mg under 260 nm excitation. The positions and intensities of UV, blue-green and red emission show a strong dependency on the ambient temperature, which was caused by the thermal quenching effect. Additionally, as the test temperature decreases, the PL peaks exhibit blue shifts and narrower full-width-at-half-maximum (FWHM) values simultaneously. The PL spectral signal of β-Ga_2O_3:Si single crystal was less affected by temperature change, indicating that the Si substitution site in a β-Ga_2O_3 crystal has high-temperature stability.

Typically, PL is a weak nonlinear effect and is used to characterize the defects in the material. Recently, Makeswaran et al. [54] demonstrated strong green-emission (~ 502 nm) characteristics with a ~30-fold enhancement in selectively engineered nanocrystalline Ga_2O_3 with control over the size, phase, and interface nanostructure. The strong emission of PL from Ga_2O_3 could be a promising option to further tune and engineer the optoelectronics performance.

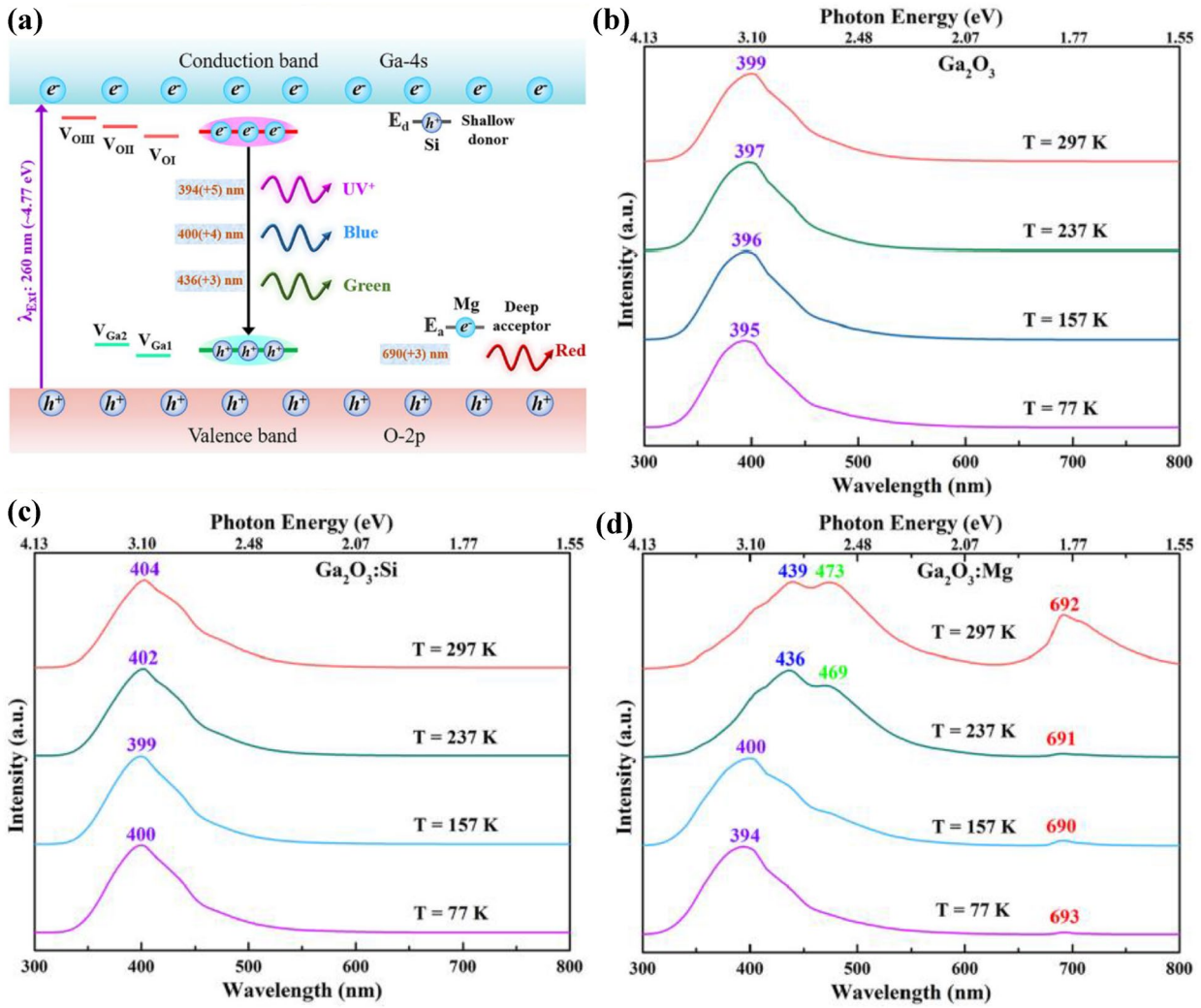

Figure 8: (a) A schematic model illustrating the estimated energy levels for selected impurities in β-Ga_2O_3. PL images of (b) un-doped β-Ga_2O_3, (c) β-Ga_2O_3:Si, and (d) β-Ga_2O_3:Mg substrates at 77 K, 157 K, 237 K, and 297 K. The excitation wavelength at 260 nm. These figures were reprinted from Ref. [45] with the permission from Elsevier.

Raman scattering

The Raman scattering is the basis of the optical Raman amplification, which has been widely used in all-optical amplification, comb generation, supercontinuum, and various optical nonlinear applications. The phonon vibrational modes obtained from the Raman and infrared spectroscopy can also be used to analyze the optical processes within a material. The Raman spectra of bulk β-Ga_2O_3 were studied by many groups [55–57]. Based on the analyses from Dohy et al. [55], Zhang et al. [50, 53], and Kranert et al. [56, 57], the irreducible representations for the acoustical and optical zone center modes in β-Ga_2O_3 are $\Gamma_{aco} = A_u + 2B_u$ and $\Gamma_{opt} = 10A_g + 5B_g + A_u + 8B_u$, respectively. Fourteen representative Raman modes were observed and can be classified into three groups. Group 1 includes $B_g(1)$, $B_g(2)$, $A_g(2)$, and $A_g(3)$, which originate from the librations and translations of chains. Group 2 includes $A_g(4)$–$A_g(6)$, representing the deformation of $Ga_I(O_I)_2$ octahedron modes. Group 3 includes $A_g(7)$–$A_g(10)$, $B_g(4)$, and $B_g(5)$, due to the stretching and bending of Ga_2O_3.

Dohy et al. [55] observed a noticeable broadening of Raman bands in the temperature range of 100–600 K when studying the Raman spectroscopy of a single-crystalline β-Ga_2O_3. It was interpreted as the result of a reversible low rate of lattice disorder caused by defects. The temperature dependence of the Raman bands frequencies and half-widths was also observed. Furthermore, Kranert et al. [56, 57] introduced a formalism to model the Raman scattering intensity for any polarization configurations for optically anisotropic crystals. A simple, depth-independent effective Raman tensor formalism can be used for integration over a sufficiently large scattering depth and point out an impact of birefringence on Raman intensities.

Zhang et al. [53] performed temperature-dependent Raman on β-Ga_2O_3 substrates doped with Si and Mg, respectively. As shown in Fig. 9, the shifting of Raman peaks indicates that tensile/bending vibrations of Ga_IO_4 tetrahedrons are easily affected by temperature. The increase in temperature causes the FWHM of the Raman scattering peak to broaden. The mechanism of this temperature effect is attributed to the broadening of temperature-dependent phonons.

Defect transition

Important evidence of inter- and intra-conduction absorption of Ga_2O_3 was recently reported by Arjan et al. [58]. The features of inter- and intra-conduction transition only appeared in doped Ga_2O_3, which indicated the mechanism involving free carriers. Figure 10a shows the transitions between and within the conduction bands of β-Ga_2O_3. The physical process is described as follows. First, free electrons undergo direct optical transitions under UV light between the different conduction bands with absorption coefficients in the range of ~ 10 cm^{-1}. Second, electrons in the lowest conduction band can transform to a higher energy state within the same conduction band. As shown in Fig. 10d–f, from the first-principle calculation, intra-conduction band absorption occurs via an indirect optical phonon with a ω^{-3} dependence in the visible to near-IR wavelength range. This frequency dependence markedly differs from the ω^{-2} dependence predicted by the Drude model of free-carrier absorption.

Arjan et al. [59] also investigated the defect-assisted recombination of photoexcited carriers in β-Ga_2O_3. The intrinsic defects, oxygen and gallium vacancies, play an important role in the temperature-independent electron capture process, as well as the temperature-dependent hole capture process. The energy levels of different nonequilibrium charge states of gallium vacancies were also analyzed at the ultrafast (sub-nanosecond) timescales [60]. Figure 10b–c show the equilibrium and nonequilibrium states in β-Ga_2O_3. These results show that the photoexcited electrons could effectively modify the permittivity and the complex refractive index of Ga_2O_3, which is important for the design of various Ga_2O_3 devices including photodetectors and high-voltage and high-speed transistors.

Photonics and optoelectronics devices

Extending the working wavelengths of photonic devices from IR to UV–Vis has been a topic of active investigation [61, 62]. The wide bandgap and outstanding electronic and optical properties have made Ga_2O_3 a very attractive candidate for the fabrication of photonic devices in the UV–Vis spectra region. To date, high-performance integrated waveguide and photodetector have been demonstrated on β-Ga_2O_3. In this section, we review the state-of-art progress in these device areas. With the rapid

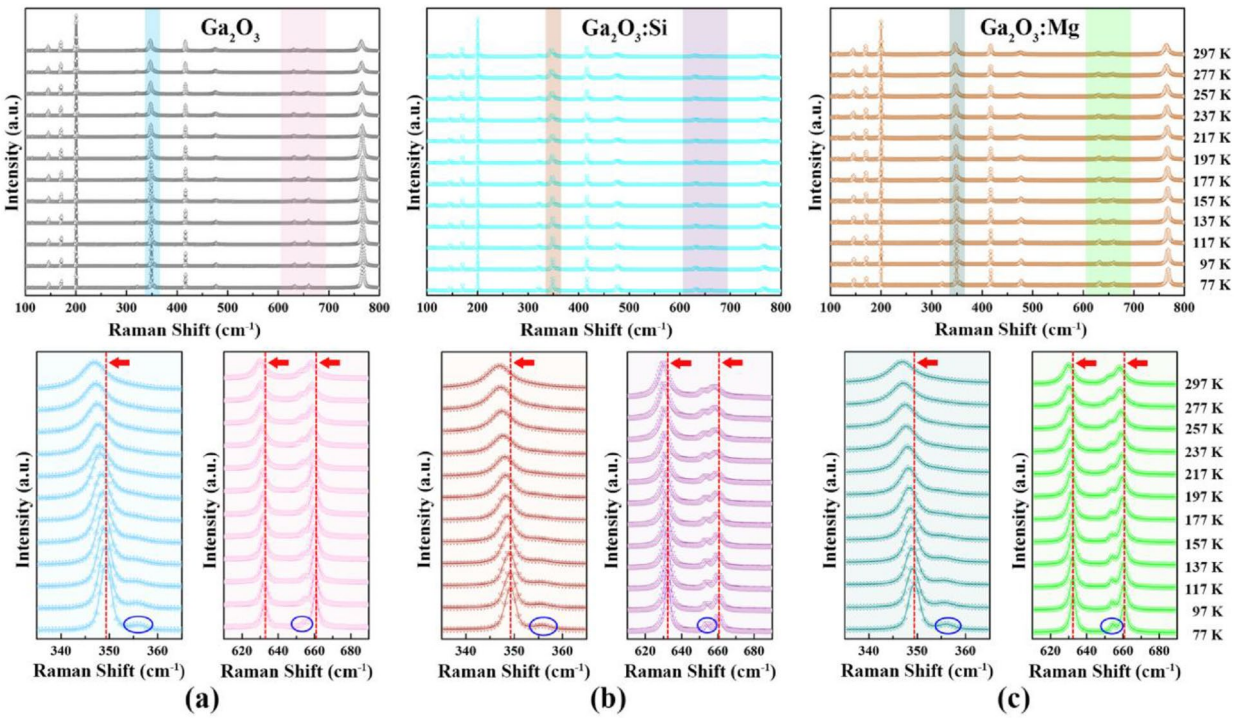

Figure 9: Raman spectra of β-Ga_2O_3 (a), β-Ga_2O_3:Si (b), and β-Ga_2O_3:Mg (c) samples in temperature from 77 to 297 K. Magnified views of the Raman spectra in the range of 335–365 cm^{-1} and 610–690 cm^{-1} (bottom). These figures were reprinted from Ref. [45] with the permission from Elsevier.

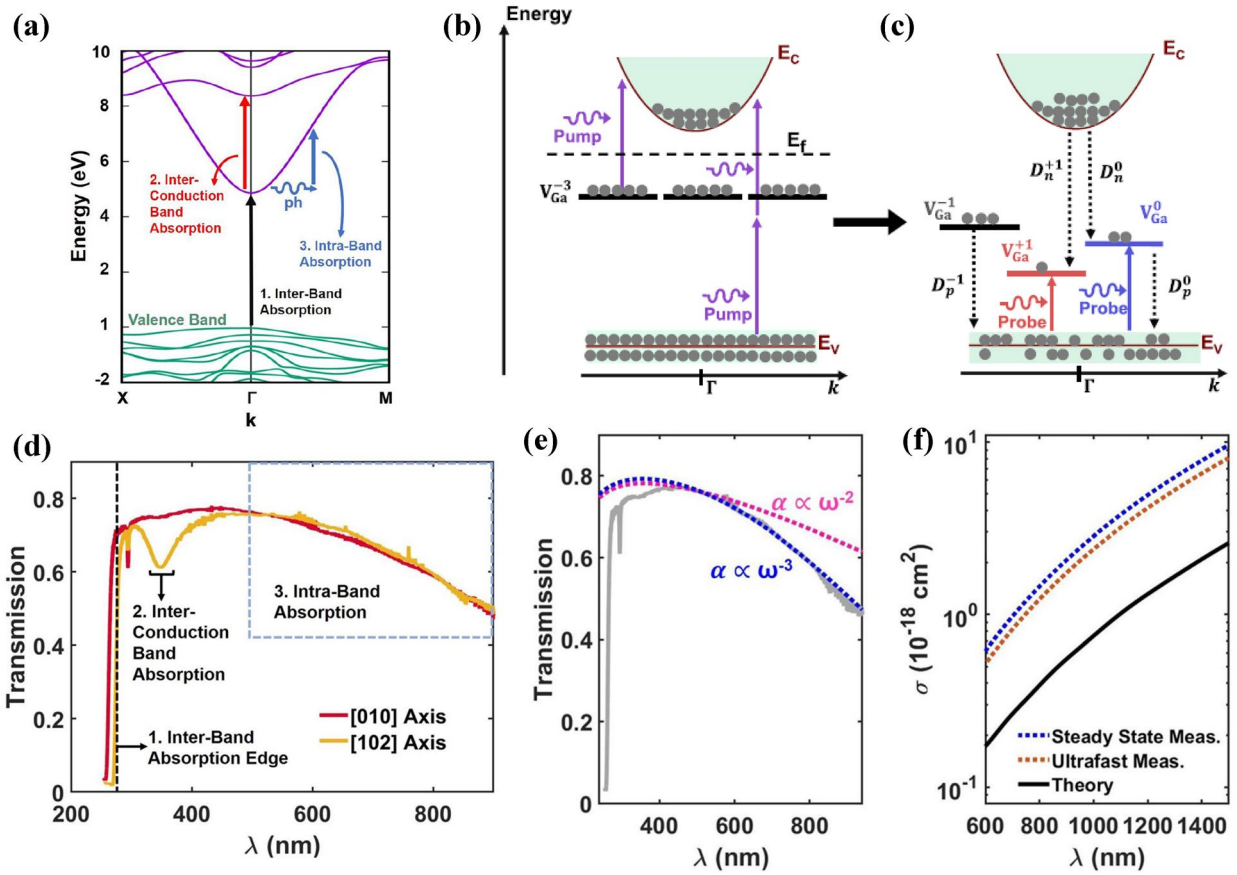

Figure 10: (a) Schematic of inter- and intra-conduction band absorption of light by conduction band electrons in β-Ga_2O_3. (b) The Ga vacancies in their equilibrium-3 charge state of n-doped β-Ga_2O_3 are depicted along with the optical excitation scheme. (c) The nonequilibrium state after the optical excitation. The Ga vacancies are present in different charge states, which allow optical transitions from the valence band. (d) Measured optical transmission of a Sn-doped β-Ga_2O_3 sample, which shows prominent features related to inter- and intra-conduction band absorption. (e) Transmission calculated assuming ω^{-3} dependence fits the data well over a broad wavelength range compared to that calculated assuming ω^{-2} (Drude model). (f) Intra-band light absorption cross sections extracted from the steady state transmission measurements and ultrafast transmission measurements, and calculated using first principles are plotted as a function of wavelength. Figure a, d–f were reprinted from Ref. [50] with the permission of AIP Publishing. Figure b–c were reprinted with permission from Ref. [52].

development of Ga_2O_3, we fully expect that more advanced devices will emerge in the next a few years for various optical and photonics applications.

Integrated waveguide

Due to the broadband transparency from the large bandgap of β-Ga_2O_3 as well as its small TPA coefficient, β-Ga_2O_3 is promising for high-performance low-loss waveguides for integrated photonics applications. Wang et al. [63] reported waveguide properties in a β-Ga_2O_3 nanowire. The as-synthesized straight nanowires present appropriate geometries for single-mode optical waveguiding, as well as favorable mechanical flexibility for micromanipulation. The measured propagation loss of the nanowire at 633 nm is on the order of 10 dB/mm.

More recently, Zhou et al. [64] report the fabrication of low loss β-Ga_2O_3 optical waveguides in the UV to NIR spectral region (Fig. 11a–e). The β-Ga_2O_3 thin films were grown on sapphire substrates using MOCVD and were fabricated into various waveguide structures using nanofabrication processes. A low propagation loss of 3.7 dB/cm was obtained on the β-Ga_2O_3 waveguide at the wavelength of 810 nm. The optimized chlorine-based inductively coupled plasma (ICP) etching was found to be critical to achieve smooth sidewalls of β-Ga_2O_3 waveguides and reduce the sidewall scattering. The high BCl_3 gas flow and ICP power led to the high plasma density, which resulted in extra etching perpendicular to β-Ga_2O_3 sidewalls. Combined with theoretical simulations, various loss mechanisms from two-photon absorption, sidewall scattering, top surface scattering, and bulk scattering, were discussed for β-Ga_2O_3 waveguides, and their contributions to the total optical loss were estimated. As shown in Fig. 11c–d, propagation losses caused by two-photon absorptions, sidewall scattering, and top surface scattering were calculated numerically. To properly model the scattering losses,

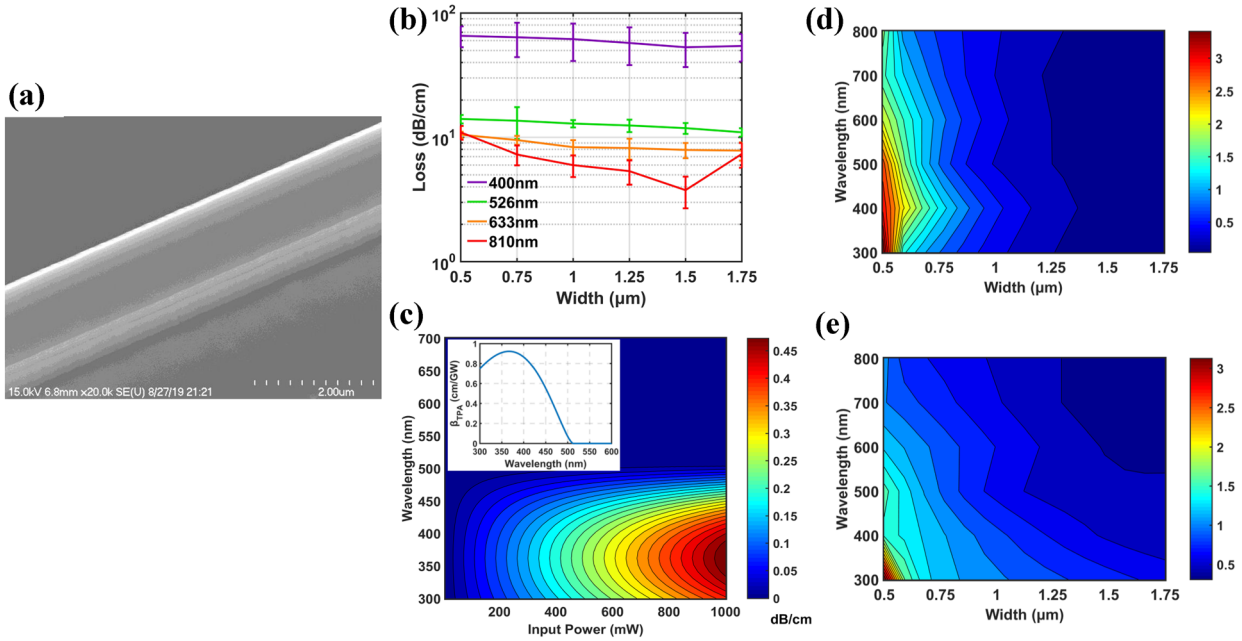

Figure 11: (a) SEM images of β-Ga_2O_3 waveguide on sapphire substrate. (b) Measured propagation loss of β-Ga_2O_3 waveguides with different widths at different wavelengths. (c) Calculated TPA loss for β-Ga_2O_3 waveguides at different wavelengths and different input powers. (Insert: theoretical TPA coefficients) (d) Calculated sidewall scattering loss for β-Ga_2O_3 waveguides. (e) Calculated top surface scattering loss for β-Ga_2O_3 waveguides. These figures were reprinted from Ref. [64], with the permission of AIP Publishing.

the volume current method was applied. Due to the 'squeezed out' effect, waveguides with smaller dimensions exhibit larger sidewall scattering loss, especially when the width is narrower than 750 nm. On the other hand, the scattering losses are also sensitive to wavelengths. The waveguides under UV light exhibit stronger scattering loss comparing with those under red light. This wavelength dependence is one of the main reasons for the dramatic increase of propagation losses of β-Ga_2O_3 waveguides at UV spectral. β-Ga_2O_3 waveguides are the fundamental basis of the optic interconnections, on-chip optical modulations and all other integrated photonic circuits. These results show that β-Ga_2O_3 is a promising optical material for the fabrication of various integrated photonic devices in the UV–NIR spectra region.

Photodetector

Since the bandgap of Ga_2O_3 is intrinsically suitable for deep UV photodetection without any doping or alloying process, the Ga_2O_3 has been widely studied for photodetector applications [65–74]. In this section, we will briefly review the progress on Ga_2O_3 photodetectors.

Pratiyush et al. [67] reported solar-blind metal–semiconductor-metal (MSM) photodetectors fabrication on MBE grown epitaxial $(\bar{2}01)$ Ga_2O_3. The detectors featured high spectral responsivity of > 1.5 A/W at 236–240 nm at a bias of 4 V with a UV to VIS rejection ratio > 10^5. The devices exhibited very low dark current < 10 nA at 20 V and showed no persistent photoconductivity as evident from the sharp transients with a high I_{photo}/I_{dark} current ratio > 10^3.

Guo et al. [69] reported a β-Ga_2O_3/NSTO (NSTO = Nb:$SrTiO_3$) heterojunction solar-blind photodetector. As shown in Fig. 12a–c, with zero power consumption, the photodetector shows a fast photoresponse time (decay time $\tau_d = 0.07$ s) and the ratio $I_{photo}/I_{dark} \approx 20$. The device also exhibits a responsivity R_λ of 43.31 A/W and an external quantum efficiency (EQE) of 2.1×10^4%. As shown in Fig. 12d–f, Kong et al. [71] fabricated a β-Ga_2O_3 Schottky structure photodetector coated by multilayer graphene. The graphene-Ga_2O_3 heterojunction device displays pronounced rectifying characteristics under deep UV light illumination. It was also revealed that the devices were highly sensitive to 254 nm UV light illumination with very good stability and reproducibility.

In addition to β-Ga_2O_3, ε-Ga_2O_3 were also investigated for photodetectors. Pavesi et al. [73] reported the undoped ε-Ga_2O_3 epitaxial films on sapphire prepared by MOCVD. The electrodes, consisting of Au (250 nm)/Ti (20 nm) bilayer, were deposited through a metal mask by thermal evaporation, followed by 10 min annealing at 500 °C. The time-dependent photo response to UV light (270 nm) under a 10 V bias voltage showed switching on ($t_{on} \sim 2$ s) and off ($t_1 \sim 0.4$ s and $t_2 \sim 2$ s). More recently, Qin et al. [12] reported ultra-high-performance MSM photodetector based on MOCVD-grown ε-Ga_2O_3 (Fig. 12g–i). A record high responsivity R of 230 A/W with a

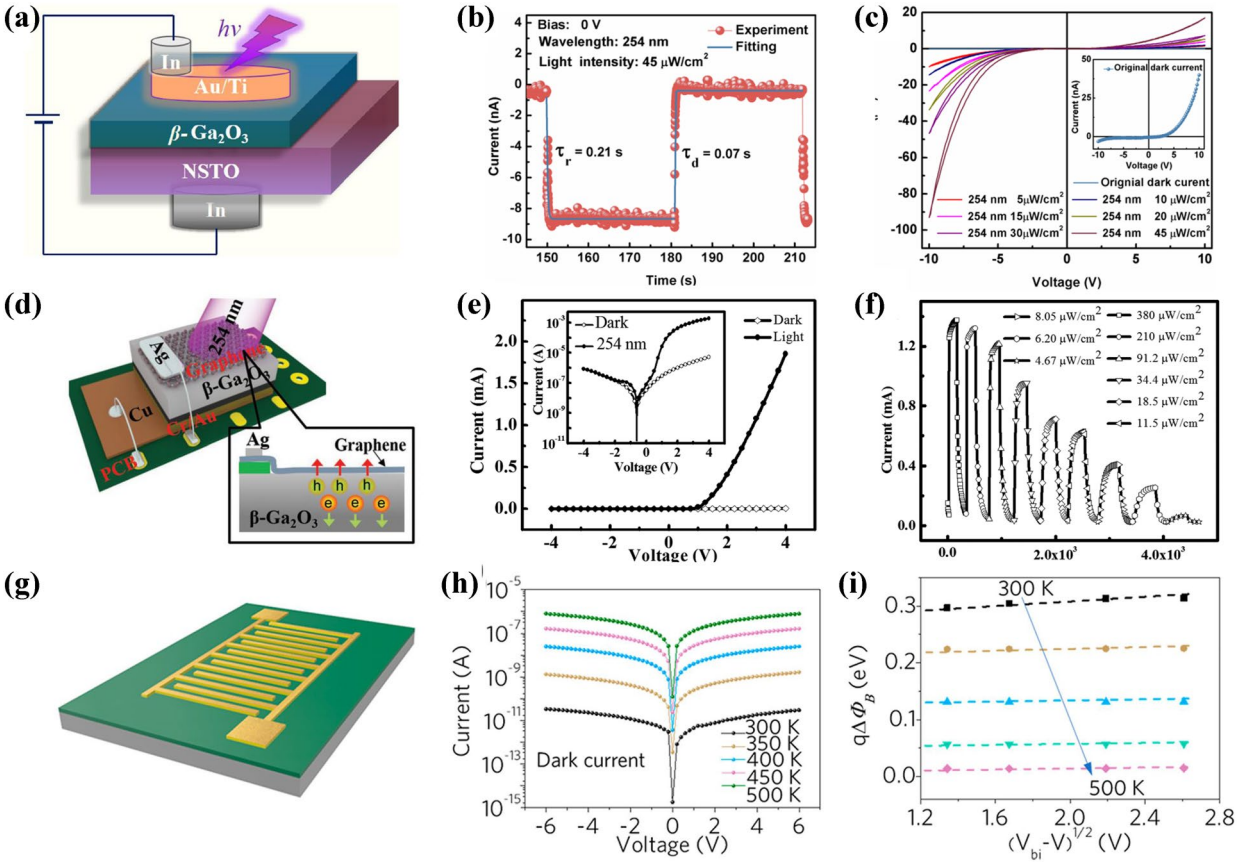

Figure 12: (a) Schematic illustration of β-Ga_2O_3/NSTO heterojunction photodetector. (b) The rise/decay edges and the corresponding exponential fitting ($\tau_r = 0.21$ s, $\tau_d = 0.07$ s) of the β-Ga_2O_3/NSTO photodetector. (c) *I–V* characteristic curves of the β-Ga_2O_3/NSTO photodetector in the dark and under 254 nm light illumination with various light intensities; the inset is the enlarged view of the fresh dark *I–V* characteristic curve. (d) Schematic diagram of the MLG/β-Ga_2O_3 wafer photodetector. (e) *I–V* characteristics of the MLG/β-Ga_2O_3 photodetector in dark and under 254 nm light irradiation, the inset shows the *I–V* curves on a logarithmic scale. (f) Photoresponse of the MLG/β-Ga_2O_3 photodetector under different light intensities. (g) Schematic illustration of the MSM ε-Ga_2O_3 photodetector. (h) *I–V* characteristic curves of the ε-Ga_2O_3 photodetector in the dark at variable temperatures. (i) Barrier height reduction versus V_{bi}–*V* with temperature increasing from 300 to 500 K. Figure a–c were reprinted with permission from Ref. [58]. Copyright (2017) American Chemical Society. Figure d–f were reprinted from Ref. [59] with the permission from John Wiley and Sons. Figure g–i were reprinted with permission from Ref. [12]. Copyright (2020) American Chemical Society.

high EQE of 1.13×10^5% at 6 V were obtained on the fabricated ε-Ga_2O_3 photodetector. A low dark current of 23.5 pA and an ultrahigh detectivity of 1.2×10^{15} Jones were achieved, suggesting the ability to sense the extremely weak signal. A record-high rejection ratio $R_{(\lambda=250\ nm)}/R_{(\lambda=400\ nm)}$ of 1.2×10^5 was obtained, indicating its high sensitivity and wavelength selectivity of light in the solar-blind spectra.

Summary

We review the recent studies on the nonlinear optical properties in Ga_2O_3, and discuss their potential applications for optical and photonic devices. With the recent development, high-quality, large-scale, and low-cost Ga_2O_3 bulk crystals and epitaxial thin films can be obtained from ECG or MOCVD method, which laid the solid foundation for their device applications. Fundamental knowledge has been obtained on the basic optical properties of β-Ga_2O_3 (which is the most stable form of Ga_2O_3), including optical energy gap, transmittance, absorption, and refractive index. Progress has also been made on the nonlinear effects in Ga_2O_3, including TPA, optical Kerr effect, photoluminescence, and Raman scattering. These nonlinear effects are critical for the development of advanced optical devices and photonic integrated circuits, which are however still not well understood for Ga_2O_3. Outstanding device performance has been obtained on loss-loss waveguide and photodetectors on both β-Ga_2O_3 and ε-Ga_2O_3. With the rapid development of Ga_2O_3 technologies, we fully expect that more advanced optics and photonics devices will emerge on this exciting new material platform, for potential UV–Vis applications in the optical computing, communication, quantum photonics, and bio-chemical sensing fields.

Acknowledgments

This work was supported by the grant from Army Research Office (ARO) PECASE Grant No. W911NF-19-1-0089, the ARO DURIP Grant No. W911NF-19-1-0129 monitored by Dr. Michael Gerhold. We gratefully acknowledge the support by Arizona State University and Rice University.

Declarations

Conflict of interest On behalf of all authors, the corresponding author states that there is no conflict of interest.

References

1. R. Konoike, K. Suzuki, S. Namiki, H. Kawashima, K. Ikeda, Opt. Express **27**, 10332 (2019)
2. W. Bogaerts, L. Chrostowski, Laser Photonics Rev. **12**, 1 (2018)
3. H. Chen, J. Zhou, D. Li, D. Chen, A.K. Vinod, H. Fu, X. Huang, T.H. Yang, J.A. Montes, K. Fu, C. Yang, C.Z. Ning, C.W. Wong, A.M. Armani, Y. Zhao, ACS Photonics **8**, 1344 (2021)
4. X. Liu, A.W. Bruch, Z. Gong, J. Lu, J.B. Surya, L. Zhang, J. Wang, J. Yan, H.X. Tang, Optica **5**, 1279 (2018)
5. S.H. Lee, D.Y. Oh, Q.-F. Yang, B. Shen, H. Wang, K.Y. Yang, Y.-H. Lai, X. Yi, X. Li, K. Vahala, Nat. Commun. **8**, 1295 (2017)
6. K.H. Li, W.Y. Fu, Y.F. Cheung, K.K.Y. Wong, Y. Wang, K.M. Lau, H.W. Choi, Optica **5**, 564 (2018)
7. X. Li, Y. Jiang, J. Li, Z. Shi, G. Zhu, Y. Wang, Opt. Laser Technol. **114**, 103 (2019)
8. A. Mohanty, Q. Li, M.A. Tadayon, S.P. Roberts, G.R. Bhatt, E. Shim, X. Ji, J. Cardenas, S.A. Miller, A. Kepecs, M. Lipson, Nat. Biomed. Eng. **4**, 223 (2020)
9. W.D. Sacher, X. Luo, Y. Yang, F.-D. Chen, T. Lordello, J.C.C. Mak, X. Liu, T. Hu, T. Xue, P. Guo-QiangLo, M.L. Roukes, J.K.S. Poon, Opt. Express **27**, 37400 (2019)
10. K. Song, H. Zhang, H. Fu, C. Yang, R. Singh (2020)
11. X. Hou, Y. Zou, M. Ding, Y. Qin, Z. Zhang (2021)
12. Y. Qin, L. Li, X. Zhao, G.S. Tompa, H. Dong, G. Jian, Q. He, P. Tan, X. Hou, Z. Zhang, S. Yu, H. Sun, G. Xu, X. Miao, K. Xue, S. Long, M. Liu, ACS Photonics **7**, 812 (2020)
13. H. Peelaers, C.G. Van de Walle, Phys. Status Solidi Basic Res. **252**, 828 (2015)
14. H. Chen, H. Fu, X. Huang, J.A. Montes, T.-H. Yang, I. Baranowski, Y. Zhao, Opt. Express **26**, 3938 (2018)
15. H.Y. Playford, A.C. Hannon, M.G. Tucker, D.M. Dawson, S.E. Ashbrook, R.J. Kastiban, J. Sloan, R.I. Walton, J. Phys. Chem. C **118**, 16188 (2014)
16. I. Cora, F. Mezzadri, F. Boschi, M. Bosi, M. Čaplovičová, G. Calestani, I. Dódony, B. Pécz, R. Fornari, CrystEngCommun **19**, 1509 (2017)
17. V. Gottschalch, S. Merker, S. Blaurock, M. Kneiß, U. Teschner, M. Grundmann, H. Krautscheid, J. Cryst. Growth **510**, 76 (2019)
18. S. Yoshioka, H. Hayashi, A. Kuwabara, F. Oba, K. Matsunaga, I. Tanaka, J. Phys. Condens. Matter **19**, 346211 (2007)
19. S.B. Cho, R. Mishra, Appl. Phys. Lett. **112**, 1 (2018)
20. M.R. Lorenz, J.F. Woods, R.J. Gambino, J. Phys. Chem. Solids **28**, 403 (1967)
21. A.S. Pratiyush, U.U. Muazzam, S. Kumar, P. Vijayakumar, S. Ganesamoorthy, N. Subramanian, R. Muralidharan, D.N. Nath, IEEE Photonics Technol. Lett. **31**, 923 (2019)
22. B. Wang, D. Look, G. Farlow, J. Phys. D. Appl. Phys. **53** (2020)
23. N. He, H. Tang, B. Liu, Z. Zhu, Q. Li, C. Guo, M. Gu, J. Xu, J. Liu, M. Xu, L. Chen, X. Ouyang, Nucl. Instruments Methods Phys. Res. Sect. A Accel. Spectrometers Detect. Assoc. Equip. **888**, 9 (2018)
24. Z. Galazka, K. Irmscher, R. Schewski, I.M. Hanke, M. Pietsch, S. Ganschow, D. Klimm, A. Dittmar, A. Fiedler, T. Schroeder, M. Bickermann, J. Cryst. Growth **529**, 125297 (2020)
25. J. Jesenovec, J. Varley, S.E. Karcher, J.S. McCloy, J. Appl. Phys. **129**, 225702 (2021)
26. H. Aida, K. Nishiguchi, H. Takeda, N. Aota, K. Sunakawa, Y. Yaguchi, Jpn. J. Appl. Phys. **47**, 8506 (2008)
27. S. Masuya, K. Sasaki, A. Kuramata, S. Yamakoshi, O. Ueda, M. Kasu, Jpn. J. Appl. Phys. **58**, 3 (2019)
28. W. Mu, Z. Jia, Y. Yin, Q. Hu, Y. Li, B. Wu, J. Zhang, X. Tao, J. Alloys Compd. **714**, 453 (2017)
29. S. Zhang, X. Lian, Y. Ma, W. Liu, Y. Zhang, Y. Xu, H. Cheng, J. Semicond. **39**, 0 (2018)
30. K. Hoshikawa, T. Kobayashi, Y. Matsuki, E. Ohba, J. Cryst. Growth **545**, 125724 (2020)
31. Y. Yao, S. Okur, L.A.M. Lyle, G.S. Tompa, T. Salagaj, N. Sbrockey, R.F. Davis, L.M. Porter, Mater. Res. Lett. **6**, 268 (2018)
32. F. Egyenes-Pörsök, F. Gucmann, K. Hušeková, E. Dobročka, M. Sobota, M. Mikolášek, K. Fröhlich, M. Tapajna, Semicond. Sci. Technol. **35**, 115002 (2020)
33. J.H. Leach, K. Udwary, J. Rumsey, G. Dodson, H. Splawn, K.R. Evans, APL Mater. **7**, 1 (2019)
34. H. Sun, K.H. Li, C.G.T. Castanedo, S. Okur, G.S. Tompa, T. Salagaj, S. Lopatin, A. Genovese, X. Li, Cryst. Growth Des. **18**, 2370 (2018)
35. T. Onuma, S. Saito, K. Sasaki, K. Goto, T. Masui, T. Yamaguchi, T. Honda, A. Kuramata, M. Higashiwaki, Appl. Phys. Lett. **108**, 1 (2016)
36. C. Zhang, F. Liao, X. Liang, H. Gong, Q. Liu, L. Li, X. Qin, X. Huang, C. Huang, Phys. B Condens. Matter **562**, 124 (2019)
37. K.A. Mengle, G. Shi, D. Bayerl, E. Kioupakis, Appl. Phys. Lett. **109**, 2 (2016)
38. T. Onuma, S. Saito, K. Sasaki, T. Masui, T. Yamaguchi, T. Honda, A. Kuramata, M. Higashiwaki, Jpn. J. Appl. Phys. **55**, 1202B2 (2016)

39. I. Bhaumik, R. Bhatt, S. Ganesamoorthy, A. Saxena, A.K. Karnal, P.K. Gupta, A.K. Sinha, S.K. Deb, Appl. Opt. **50**, 6006 (2011)
40. F. Ricci, F. Boschi, A. Baraldi, A. Filippetti, M. Higashiwaki, A. Kuramata, V. Fiorentini, R. Fornari, J. Phys. Condens. Matter. **28**, 224005 (2016)
41. F. Zhang, H. Li, Y.T. Cui, G.L. Li, Q. Guo, AIP Adv. **8**, 1 (2018)
42. S.J. Hao, M. Hetzl, F. Schuster, K. Danielewicz, A. Bergmaier, G. Dollinger, Q.L. Sai, C.T. Xia, T. Hoffmann, M. Wiesinger, S. Matich, W. Aigner, M. Stutzmann, J. Appl. Phys. **125**, 105701 (2019)
43. K. Goto, H. Nakahata, H. Murakami, Y. Kumagai, Appl. Phys. Lett. **117**, 2 (2020)
44. A. Kovach, D. Chen, J. He, H. Choi, A.H. Dogan, M. Ghasemkhani, H. Taheri, A.M. Armani, Adv. Opt. Photon. **12**, 135 (2020)
45. M.A. Arshad, A. Hartung, M. Jäger, Laser Phys. Lett. **16**, 35108 (2019)
46. S. Armaghani, S. Khani, M. Danaie, Superlattices Microstruct. **135**, 106244 (2019)
47. X. Liu, C. Sun, B. Xiong, L. Wang, J. Wang, Y. Han, Z. Hao, H. Li, Y. Luo, J. Yan, T. Wei, Y. Zhang, J. Wang, Appl. Phys. Lett. **113**, 1 (2018)
48. M. Sheik-Bahae, D.C. Hutchings, D.J. Hagan, E.W. Van Stryland, IEEE J. Quantum Electron. **27**, 1296 (1991)
49. W. Mi, J. Ma, C. Luan, H. Xiao, J. Lumin. **146**, 1 (2014)
50. K. Zhang, Z. Xu, S. Zhang, H. Wang, H. Cheng, J. Hao, J. Wu, F. Fang, Phys. B Condens. Matter **600**, 412624 (2021)
51. G. Naresh-Kumar, H. MacIntyre, S. Subashchandran, P.R. Edwards, R.W. Martin, K. Daivasigamani, K. Sasaki, A. Kuramata, Phys. Status Solidi Basic Res. **258**, 1 (2021)
52. M. Yamaga, T. Ishikawa, M. Yoshida, T. Hasegawa, E.G. Villora, K. Shimamura, Phys. Status Solidi Curr. Top. Solid State Phys. **8**, 2621 (2011)
53. K. Zhang, Z. Xu, J. Zhao, H. Wang, J. Hao, S. Zhang, H. Cheng, B. Dong, J. Alloys Compd. **881**, 160 (2021)
54. N. Makeswaran, D. Das, V. Zade, P. Gaurav, V. Shutthanandan, S. Tan, C.V. Ramana, A.C.S. Appl, Nano Mater. **4**, 3331 (2021)
55. D. Dohy, G. Lucazeau, A. Revcolevschi, J. Solid State Chem. **45**, 180 (1982)
56. C. Kranert, C. Sturm, R. Schmidt-Grund, M. Grundmann, Sci. Rep. **6**, 1 (2016)
57. C. Kranert, C. Sturm, R. Schmidt-Grund, M. Grundmann, Phys. Rev. Lett. **116**, 1 (2016)
58. A. Singh, O. Koksal, N. Tanen, J. McCandless, D. Jena, H. Xing, H. Peelaers, Appl. Phys. Lett. **117**, 072103 (2020)
59. O. Koksal, N. Tanen, D. Jena, H. Xing, F. Rana, Appl. Phys. Lett. **113**, 252102 (2018)
60. A. Singh, O. Koksal, N. Tanen, J. McCandless, D. Jena, H. Xing, H. Peelaers, F. Rana, Phys. Rev. Res. **3**, 1 (2021)
61. C. Huang, H. Zhang, H. Sun, Nano Energy **77**, 105 (2020)
62. H. Zhang, C. Huang, K. Song, H. Yu, C. Xing, D. Wang, Z. Liu, H. Sun, Rep. Prog. Phys. **84**, 044401 (2021)
63. F. Wang, Z. Han, L. Tong, Phys. E Low-Dimensional Syst. Nanostructures **30**, 150 (2005)
64. J. Zhou, H. Chen, H. Fu, K. Fu, X. Deng, X. Huang, T.H. Yang, J.A. Montes, C. Yang, X. Qi, B. Zhang, X. Zhang, Y. Zhao, Appl. Phys. Lett. **115**, 251108 (2019)
65. T. Oshima, T. Okuno, N. Arai, N. Suzuki, S. Ohira, S. Fujita, Appl. Phys. Express **1**, 011202 (2008)
66. T. Oshima, T. Okuno, S. Fujita, Jpn. J. Appl. Phys. Part 1 Regul. Pap. Short Notes Rev. Pap. **46**, 7217 (2007)
67. A. SinghPratiyush, S. Krishnamoorthy, S. VishnuSolanke, Z. Xia, R. Muralidharan, S. Rajan, D.N. Nath, Appl. Phys. Lett. **110**, 1 (2017)
68. J. Wang, L. Ye, X. Wang, H. Zhang, L. Li, C. Kong, W. Li, J. Alloys Compd. **803**, 9 (2019)
69. D. Guo, H. Liu, P. Li, Z. Wu, S. Wang, C. Cui, C. Li, W. Tang, ACS Appl. Mater. Interfaces **9**, 1619 (2017)
70. D. Guo, Y. Su, H. Shi, P. Li, N. Zhao, J. Ye, S. Wang, A. Liu, Z. Chen, C. Li, W. Tang, ACS Nano **12**, 12827 (2018)
71. W.Y. Kong, G.A. Wu, K.Y. Wang, T.F. Zhang, Y.F. Zou, D.D. Wang, L.B. Luo, Adv. Mater. **28**, 10725 (2016)
72. X.C. Guo, N.H. Hao, D.Y. Guo, Z.P. Wu, Y.H. An, X.L. Chu, L.H. Li, P.G. Li, M. Lei, W.H. Tang, J. Alloys Compd. **660**, 136 (2016)
73. M. Pavesi, F. Fabbri, F. Boschi, G. Piacentini, A. Baraldi, M. Bosi, E. Gombia, A. Parisini, R. Fornari, Mater. Chem. Phys. **205**, 502 (2018)
74. S. Ahn, F. Ren, S. Oh, Y. Jung, J. Kim, M.A. Mastro, J.K. Hite, C.R. Eddy, S.J. Pearton,J. Vac. Sci. Technol. B Nanotechnol. Microelectron. Mater. Process. Meas. Phenom. **34**, 207 (2016)
75. M. Marezuo, J.P. Remeika, J. Chem. Phys. **46**, 1862 (1967)
76. F. Mezzadri, G. Calestani, F. Boschi, D. Delmonte, M. Bosi, R. Fornari, Inorg. Chem. **55**, 12079 (2016)
77. R. Roy, V.G. Hill, E.F. Osborn, J. Am. Chem. Soc. **74**, 719 (1952)